

# **A new concept of a two-dimensional supersonic relative inlet mach number compressor cascade**

**Toyotaka Sonoda, Markus Olhofer, Toshiyuki Arima,  
Bernhard Sendhoff**

**2008**

**Preprint:**

This is an accepted article published in Proc. of the ASME Turbo Expo, June 8-12, 2009, Orlando, FL USA. The final authenticated version is available online at: [https://doi.org/\[DOI not available\]](https://doi.org/[DOI not available])

GT2009-59926

## A NEW CONCEPT OF A TWO-DIMENSIONAL SUPERSONIC RELATIVE INLET MACH NUMBER COMPRESSOR CASCADE

**Toyotaka Sonoda**

Aircraft Engine R&D Center,  
 Honda R&D Co.  
 Wako-shi, Saitama 351-0193, Japan

**Markus Olhofer**

Honda Research Institute Europe GmbH  
 Carl-Legien-Str.30  
 D-63073 Offenbach/Main, German

**Toshiyuki Arima**

Fundamental Technology Research Center,  
 Honda R&D Co.  
 Wako-shi, Saitama 351-0193 Japan

**Bernhard Sendhoff**

Honda Research Institute Europe GmbH  
 Carl-Legien-Str.30  
 D-63073 Offenbach/Main, Germany

### ABSTRACT

In this study, a numerical shape optimization method based on evolutionary algorithms coupled with a verified CFD solver has been applied to the ambitious target of a shock free 2-D supersonic inlet Mach number compressor cascade. The study is based on the DLR-PAV-1.5 supersonic compressor cascade designed by the pre-compression blading concept. The DLR cascade airfoil has been optimized using a verified CFD code. A superior performance of the optimized supersonic cascade with about 24% reduction of the total pressure loss coefficient compared to the original cascade has been realized. The flow mechanisms observable around the blade with improved performance and the resulting design concept are discussed in this paper.

### NOMENCLATURE

AVDR	axial velocity density ratio = $(\rho_2 w_2 \sin \beta_2) / (\rho_1 w_1 \sin \beta_1)$
c	chord length
M	Mach number
p	pressure
Re	Reynolds number based on chord length
r	normalized radius length by chord length
s	blade spacing
t	airfoil thickness
x	axial chord-wise coordinate
y	pitch-wise (tangential) coordinate
$y^+$	normalized distance from wall = $y(\tau_w/\rho)^{1/2}/\nu$

$\beta$	flow angle with respect to cascade front
$\omega$	total pressure loss coefficient = $(p_{t1} - p_{t2}) / (p_{t1} - p_1)$

### Additional nomenclature for optimization

$\vec{x}$	object parameter vector to be optimized
$\sigma$	standard deviation of mutation steps in ES
$\tau$	adaptation rate of the standard deviation $\sigma$
n	search space dimension (number of object parameter)
$\vec{z}$	vector of normally distributed random numbers
$t_i$	quality criteria
$\eta_i$	criteria weighting coefficients
$\mu$	number of parent individuals
$\lambda$	number of offspring individuals
Q	objective function

### Abbreviations

CFD	computational fluid dynamics
EXP	experiment
LE	leading edge
TE	trailing edge
ES	evolutionary strategy

### Subscripts

1	inlet plane, 150mm upstream from LE
2	exit plane, 25mm downstream from TE
ax	axial
t	total

## INTRODUCTION

Three-dimensional design techniques, e.g. blade sweep and lean stacking, are widely used in modern civil aero engines in order to improve their performance. Especially the fan rotor, located at the engine front side, has a very complex three dimensional geometry resulting from sweep and/or lean technologies. The general “blade sweep” concept to reduce the component of the Mach number perpendicular to the shock face, and thereby the shock loss, is known since more than sixty years. However, workable blade sweep applications in turbomachinery design have only recently been introduced.

According to previous research results, forward swept rotors seem to be superior to unswept rotors and aft swept rotors for both low and high speed flow fields. For example, in the case of the subsonic regime without a shock wave Mohammed and Raj [1] experimentally demonstrated the benefit of the forward swept rotor in a very low speed environment.

Wadia et al. [2] investigated the effects of sweep and lean on a highly loaded fan in the transonic regime with a tip relative Mach number range between 1.5 to 1.6 using a combination of experiment and CFD. They found that all swept rotors demonstrated a peak stage efficiency level that was equal to the unswept rotor, but the forward swept rotor achieved the highest rotor-alone peak efficiency. They also found that the forward swept design significantly improved the stall margin.

Denton and Xu [3] also investigated the effect of lean and sweep on transonic fan performance with a tip relative inlet Mach number of about 1.5, using their 3D multistage viscous solver. Overall, they found that very little change in peak efficiency or pressure ratio is generated by blade sweep or lean although there are significant effects on stall margin for the forward swept rotor. They also reported that it is important to ensure that the bow shock and the passage shock remain distinct and do not merge in the outer part of the span. It is also seen that in the blade to blade plane a strong normal shock near the pressure surface generates a locally high loss and should be avoided. They concluded that these features are more easily achieved by very careful design of the blade sections and hub and casing profiles than by changes of the stacking.

In summary, it seems to be difficult to reduce shock and/or shock-boundary layer interaction losses using a forward swept blade. Therefore, it seems to be worthwhile to investigate the shock characteristics of two-dimensional cascades designed using numerical shape optimization methods based e.g. on evolutionary algorithms (Beyer and Schwefel [4]).

So far, numerical shape optimization methods have been successfully applied to compressor and turbine cascades and new design concepts have been discovered. For example, it has been found that an extreme front loaded compressor airfoil cascade has superior performance to CDA (controlled diffusion airfoil) in the low Reynolds number regime for both subsonic

and transonic regimes (Sonoda et al. [5], [6]). Furthermore, it has been demonstrated that, for turbine blades, a double shock system is effective to reduce the shock loss. A turbulent boundary layer generated by the optimization does not show boundary layer separation due to the shock-boundary layer interaction (Sonoda et al. [7]).

The main objective of this research is to investigate the 2-D supersonic flow field with shock waves and to find out whether a new design concept can be discovered using a numerical optimization method.

There are typically two design methods for supersonic rotor blades (Morris et al., [8]). The first one is “multiple-circular-arc design” (MCA) which is more flexible with regard to the airfoil shape than “double circular-arc” (DCA) design and has been applied to supersonic rotor blades. The suction surface curvature of the front camber region is reduced to suppress acceleration in front of the passage entrance in order to weaken the normal shock wave. The second method is the “pre-compression blade design” which is applied for inlet Mach numbers higher than 1.3. It leads to a concave suction-surface curvature around the frontal chord in order to generate a series of compression waves which diffuse the supersonic flow. The pre-compression wave system lowers the Mach number of the flow across the passage entrance, reducing the total pressure loss associated with the first oblique passage shock and the second normal passage shock.

## METHOD AND APPROACH

### Cascade Model

The cascade model to be optimized in this research is the DLR-PAV-1.5 supersonic compressor cascade tested at DLR by Schreiber [9]. The pre-compression blading has been designed especially to investigate shock/boundary layer interaction. The geometry is typical for a tip section of a highly loaded transonic fan operating with an axial Mach number of 0.6 and a relative inlet Mach number of 1.5.

The geometry and the cascade design parameters are shown in Fig. 1 and Table 1, respectively. The cascade has a static pressure ratio of more than 2.0 with relatively small flow turning. In order to reduce the Mach number incident to the shock-wave at the blade passage entrance, the profile was designed with a negative suction surface camber along the cascade entrance portion (about 5 degrees within 18% of chord). Thereby, the surface velocity is reduced isentropically to a Mach number level of around 1.4 over the main part of the blade passage entrance. This so-called “pre-compression design” considerably reduces the losses resulting from the detached bow-shock and the first shock at the blade passage entrance. The design was found by prescribing the supersonic Mach number distribution on the blade suction surface entrance region up to a position where the oblique passage shock meets the blade surface.

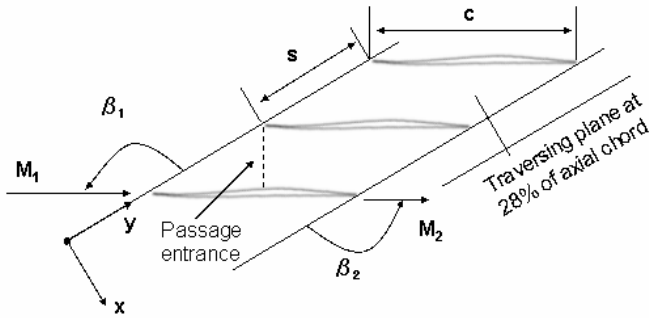


**Fig. 1 Definition of the cascade geometry obtained from Schreiber and Starken [10] and Küsters et al. [11].**

**Table 1 Cascade design and geometry parameters for DLR-PAV-1.5; “baseline” cascade**

Inlet relative Mach number: $M_1$	1.5
Inlet relative flow angle: $\beta_1$ (deg)	150
Static pressure ratio:	2.15
Flow turning angle ( deg )	3
Chord: $c$ (mm)	170
Maximum thickness: $t_{max}/c$	0.035
LE radius spacing: $r/c$	0.0025
Pitch-chord ratio: $s/c$	0.65
Stagger angle: $\beta_s$ ( deg )	148.1
Reynolds number: $Re$	$2.6 \times 10^6$

## Design Optimization with Evolutionary Algorithms

In order to optimize the blade geometry an evolutionary algorithm is applied, which belongs to the class of global stochastic optimization algorithms. In this work, a variant of evolutionary algorithms called Evolutionary Strategy (ES) is used which has proven to be highly efficient for the optimization of continuous object parameter values. Like most evolutionary algorithms, ES are population based and operate cyclic from generation to generation. During one evolutionary cycle individuals of a population of solutions are reproduced, mutated (and recombined) and selected after the evaluation of their quality.

In the classical form of Evolutionary Strategies the variations are generated by adding random numbers drawn from a normal distribution  $N(0, \sigma^2)$  with a mean value of zero and standard deviation  $\sigma$  to the variables describing a possible solution. The standard deviation  $\sigma$  of the distribution is adapted with a so-called mutative self-adaptation strategy during the search and is, in opposite to most other evolutionary algorithms, encoded in the individual.

Several variants of Evolutionary Strategies have been proposed to improve the performance of the classical Evolution Strategy.

Since the standard deviation, which can be interpreted as a step size has a high influence on the performance, its adaptation is the focus of a large number of proposed algorithms.

One of the earliest variations took into account that step sizes for different directions in the search space should be adapted independently from each other when the parameters scale differently. Additionally, correlated changes of object parameters should be possible. In the latter case, the full covariance matrix, i.e. of the order of  $n^2$  parameters, of the normal distribution has to be adapted. In order to achieve this, stochastic fluctuations during the adaptation process have to be kept under control and adaptation has to be stabilized. Therefore, methods (e.g. CMA-ES, [12], [13]) have been formulated which integrate information about the history of the optimization process and which adapt the covariance matrix based on realized and successful variations instead of applying random modifications. The Covariance Matrix Adaptation Evolutionary Strategy (CMA-ES) has been successfully applied, e.g. by the authors [14], to the optimization of turbine blade designs.

Another common method in the field of design optimization is to use surrogate or approximation models to reduce the number of costly performance evaluations. They are related to response surface methods which have a long history in experimental optimization. The underlying idea is to build approximation models based on already evaluated solutions, to replace the original quality function by the approximation model for some evaluations during search and thereby to combine simulation and approximation. Several publications report the efficiency of these methods [15], [16], [17].

The main idea behind most of these extensions is to acquire information about the structure of the local quality function and to use this to bias the generation of new solutions and to increase the evaluation efficiency. Many of the proposed methods increase the convergence speed of the algorithm and enable the application of evolutionary search methods to a large variety of design optimization problems.

However, the more the algorithm relies on knowledge about the local quality function, the higher is the risk of converging to a local optimum due to the bias towards expected maxima based on earlier calculations or prior knowledge. Unfortunately, up to now there is no theory available on how stochastic optimization algorithms work most efficiently on multi-modal problems and we are left with an empirical weighting between the exploration and the exploitation side of optimization. The probability to identify a global optimum in a multimodal search space cannot be properly evaluated and strongly depends on the actual search space.

Besides the balance between exploitation and exploration, an important element of modern numerical optimization algorithms is robustness and the ability to cope with noisy

quality evaluations [18]. Here it has been shown that the more sophisticated methods like CMA-ES can have problems [19].

In summary, whether the higher performing (with respect to convergence speed) advanced adaptation and approximation methods are used or whether a high degree of stochasticity is maintained depends on the actual objective of the optimization process and the answer is not as clear-cut as it superficially seems.

In this work, we have aimed at discovering new design principles and therefore wanted to realize a higher degree of exploration and a better coverage of the search space being aware that this means additional expensive quality evaluations (which is relieved by the fast CFD solver, see next section) and reduced convergence speed.

Therefore a comparably simple evolutionary strategy is applied which relies on the adaptation of only one single global step size which is mutatively adapted. That means that an individual consists of an object parameter vector  $\bar{x}$  and one single standard deviation  $\sigma$ . A mutation is described by two steps. At first the standard deviation at time step  $t$  is modified by  $\sigma^{t+1} = \sigma^t e^{r \cdot z}$ . This way, the standard deviation  $\sigma^{t+1}$  at time step  $t+1$  is generated by a random variation (log-normally distributed,  $z$  is normally distributed) of the standard deviation  $\sigma^t$  of the previous time step. The optimization parameter  $\tau$  can be interpreted as an adaptation rate of the step size and is set here to a standard value of  $\tau = 1/\sqrt{2n}$  with  $n$  denoting the dimensionality of the optimization problem. In a second step, the object parameter values describing a blade are generated by adding a random vector  $\bar{z} \sim N(0, \sigma^2)$  whose elements are drawn from a normal distribution. Therefore, the information about the local quality function that is used in this algorithm is the estimation of one optimal step size and the current optimal position in the search space.

After the evaluation of each individual in the population the best  $\mu$  individuals from the  $\lambda$  (offspring) individuals are selected to form the parent population for the following generation  $t+1$ . This is referred to as  $(\mu, \lambda)$ -selection in ES. In this work, we have not used a recombination operator, because in our experience recombination is often too disruptive for design optimization problems.

### Blade profile definition

The blade contour is encoded by a closed non-uniform third order rational B-spline, as shown in Fig. 2. The control point coordinates (called object parameters in the previous section) are subject to optimization. In this optimization, the object parameter vector consists of 20 spline control points, where each control point is represented by the  $x$  and  $y$  coordinate. Therefore, in total 40 object parameters are optimized. For the optimization, the real chord length and the solidity are fixed by design requirements.

### Objective function

The quality of a design is described by five criteria evaluating the pressure loss  $\omega$  of the design, the deviation angle  $\alpha$  and three thickness values, which are chosen heuristically to allow a comparison of the generated blade shape with the given design described in [9]. Besides the criterion evaluating the pressure loss all other criteria can be seen as constraints of the design. In case the constraint for the outlet flow angle or a geometric constraint is violated the criteria have the effect of a penalty term.

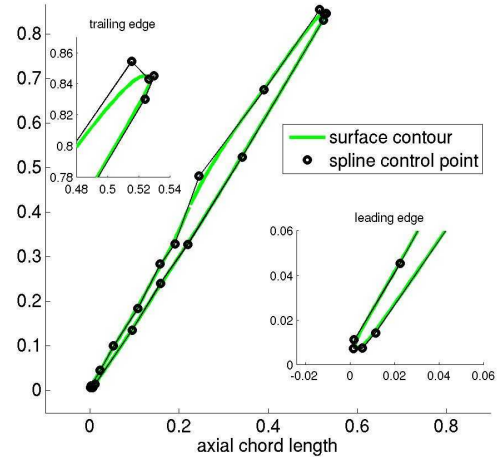


Fig. 2 Airfoil representation by spline control points.

Therefore, a simple aggregation by a weighted sum approach generating the overall quality  $Q$  is applied as follows:

$$\begin{aligned}
 t_1 &= \omega \\
 t_2 &= \max(0, |\beta_2 - \beta_{2,\text{design}}| - \delta\beta) \\
 t_3 &= \max(0, r_{\text{LE},\text{design}} - r_{\text{LE}}) \\
 t_4 &= \max(0, r_{\text{TE},\text{design}} - r_{\text{TE}}) \\
 t_5 &= \max(0, \Theta_{\text{min},\text{design}} - \Theta_{\text{min}}) \\
 Q &= \sum_{i=1}^5 \eta_i t_i
 \end{aligned}$$

The following constraints are defined:

$$\begin{aligned}
 \text{outlet flow angle} \quad \beta_{2,\text{design}} &= 151^\circ \pm \delta\beta \\
 \text{minimal radius at leading edge: } r_{\text{LE},\text{design}} &= 0.0022 \\
 \text{minimal radius at trailing edge: } r_{\text{TE},\text{design}} &= 0.0037 \\
 \text{minimal thickness: } \Theta_{\text{min},\text{design}} &= 2r_{\text{TE},\text{design}}
 \end{aligned}$$

The weights  $\eta_i$  are chosen in such a way that the constraints described by criteria  $t_2$  up to  $t_5$  dominate the quality function as soon as they are different from zero, i.e. as soon as the

constraints are violated. The values are set empirically to  $\eta_1 = 1$ ,  $\eta_2 = 10$  and  $\eta_{3...5} = 10^4$  resulting in feasible solutions early in the design process. The results that are presented here are from an optimization run with an offspring population of  $\lambda = 10$  individuals and  $\mu = 2$  parents: (2,10)-ES. The algorithm has been stopped after about 200 generations (2000 CFD evaluations).

### Flow Solver

A quasi-three-dimensional (Q3D) version of the Navier-Stokes flow solver, HSTAR (Honda Software for Turbomachinery Aerodynamics Research) (Arima et al. [20]) has been used with the condition of AVDR=1.0 (stream-tube thickness is constant). The flow solver had previously been successfully applied to both turbine and compressor cascades.

HSTAR can be configured to run in a fast mode during the optimization and in a high precision mode for the detailed flow analysis after the optimization. The computational grids for the optimization and the detailed flow analysis have the following sizes 251 x 81 and 301 x 91 (“stream-wise” x “pitch-wise” directions), respectively. The average values of  $y^+$  near the wall for both modes are of the order of 1.0 for using the low Reynolds k- $\epsilon$  turbulence model proposed by Chien [21].

For the detailed flow analysis, the grid number has been increased in order to achieve a higher resolution, especially, for the shock pattern in the free stream region. Figure 3 shows the computational grid used for the detailed flow analysis. The stream-wise 150 nodes are positioned on the airfoil surface.

During the optimization the exit static pressure is fixed. As a result, the inlet Mach number or the inlet flow angle can slightly deviate from the target value depending on the geometry of the frontal suction surface of the optimized airfoil. In the detailed flow analysis, the exit static pressure (back pressure) is adjusted so that the computed inlet Mach number equals the target value.

For the validation, experimental data by Schreiber [22] and Küsters and Schreiber [11] have been used. Although the cascade inlet Mach number is supersonic, the airfoil stagger angle is high, so the axial component of the inlet velocity is subsonic. This gives rise to the “unique incidence” condition where there exists a fixed relationship between inlet Mach number and inlet flow angle. Therefore, for the boundary condition it is not possible to specify both values. In this study, the total pressure, the total temperature, and the pitch-wise velocity are given as the inlet boundary conditions.

## RESULTS AND DISCUSSIONS

### Validation and Flow Mechanism for Baseline Cascade

A summary of the input parameters and the computed (CFD) and experimental (EXP) flow parameters for the “baseline” cascade is shown in Table 2 (see “EXP” and “CFD-

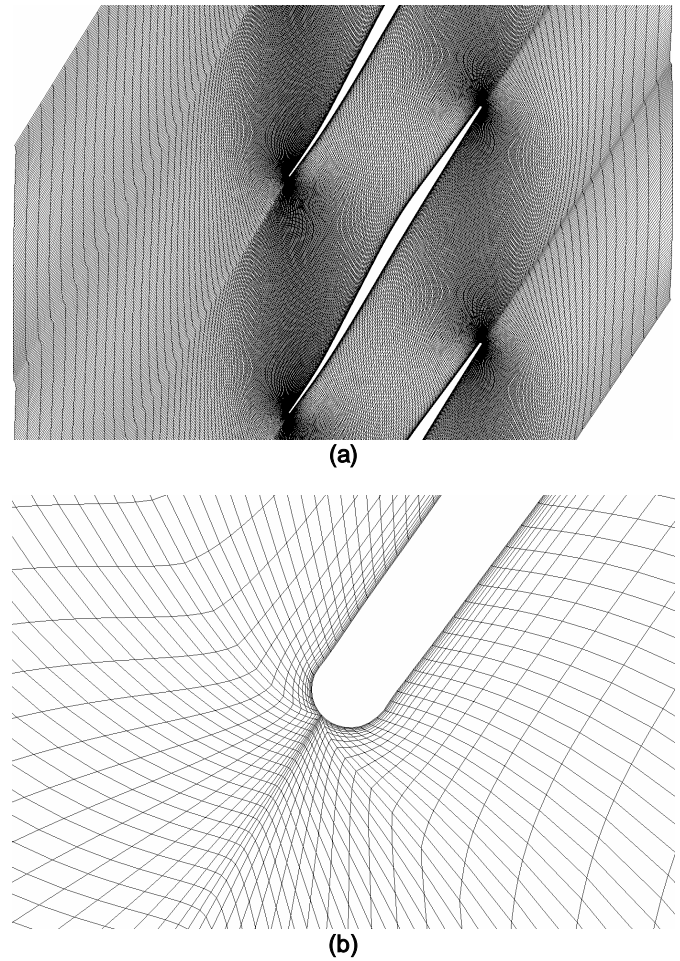


**Fig. 3 Computational grid, (a) overall, (b) leading edge part in detail.**

**Table 2 Comparison of computed flow parameters with experimental results**

Flow parameters	EXP	CFD	
		Baseline	Optimized
Inlet total temperature, [K]	319.0	←	←
Inlet total pressure, $P_{t1}$ [Pa]	120000	←	←
Inlet Mach number, $M_1$	1.45	1.457	1.508
Inlet flow angle, $\beta_1$ [deg]	150.22	150.28	149.24
Outlet Mach number, $M_2$	0.72	0.734	0.789
Outlet flow angle, $\beta_2$ [deg]	149.10	148.6	150.4
Static pressure ratio	2.21	2.22	2.31
Loss coefficient:	0.112	0.114	0.087
AVDR	1.01	1.00	1.00
Re	$2.7 \times 10^6$	←	←

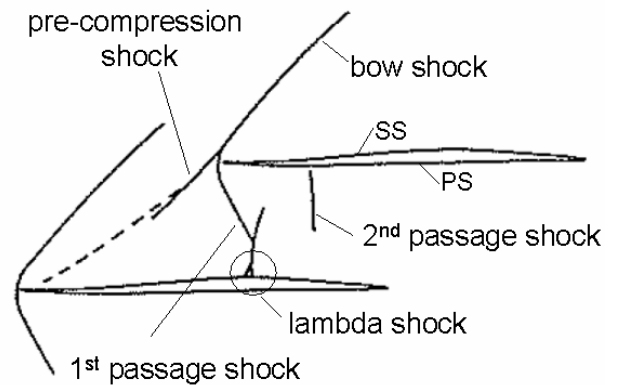
Baseline”). In general, there is a very good agreement between CFD and EXP.

Figure 4 shows the experimental shock wave pattern, obtained from a sketch of the real shock-wave pattern (Schlieren picture) at a slightly lower Mach number (1.45) than the design inlet Mach number of 1.5 (Schreiber [10]). There is a relatively strong first oblique passage shock which induces a boundary layer separation on the blade suction surface, forming a small lambda shock above the separation region. The pressure surface shows acceleration along the front portion up to a Mach number of 1.14 (see Fig. 6 EXP) ahead of the second nearly normal passage shock, which meets the pressure surface at about 20% of chord. In Fig. 4, we also observe a unique feature of the pre-compression blade design, i.e., coalescence of the left-running characteristics, emanating from the concave forward portion of the blade suction surface, which overlaps and forms a so-called pre-compression shock-wave. This shock-wave intersects the detached bow shock of the adjacent blade. As Schreiber [10] has reported the pre-compression shock is relatively weak, but it reduces the Mach number along the suction surface around the frontal portion, and, as a result, the passage entrance Mach number is reduced from about 1.7 to 1.35 (see Fig. 6 EXP).

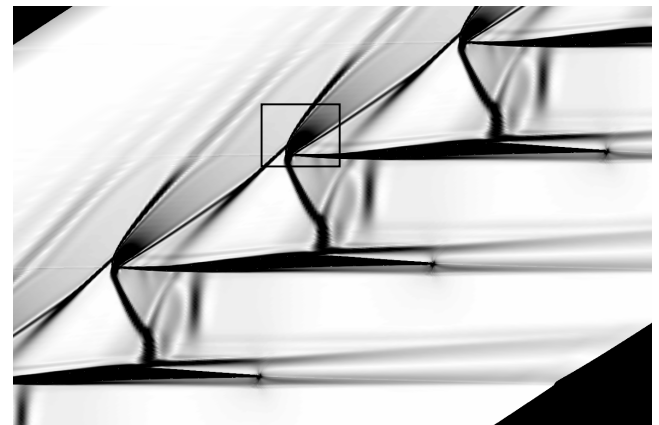
Figure 5 (a) shows the simulated Schlieren picture for the “baseline” cascade obtained from a shading picture of computed density gradient magnitudes. The bow shock, the first passage shock, the second passage shock, and the pre-compression shock observed in the experiment (see Fig. 4) are clearly captured by the CFD calculation. A severe boundary layer separation on the suction surface at around 60% chord occurs due to the first passage shock/boundary layer interaction, although the lambda shock observed in the experiment is not clearly visible in CFD.

In general, the simulated Schlieren picture is very similar to the experimental one in Fig. 4. Both the expansion waves as well as the pre-compression waves along the leading edge suction surface portion are observed in CFD, as shown in Fig. 5 (b). We notice an intersection of the pre-compression shock with the bow shock. A stable shear layer downstream of the shock interaction point develops and remains about a certain distance from the suction surface (see dashed line in Fig. 5 (b)). This physical behavior has also been reported by Küsters and Schreiber [11].

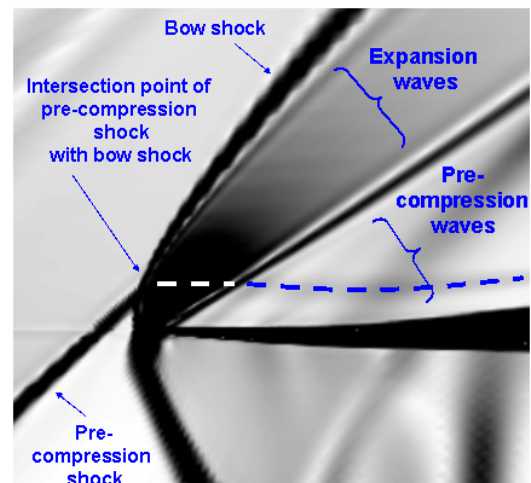
Figure 6 shows the comparison of the measured and the calculated isentropic airfoil surface Mach number distribution. The experimental data has been taken from Schreiber [22]. In general, the quantitative agreement between the shock positions and strength is poor whereas the values for the overall performance are very close, see Table 2 “EXP” and “CFD-Baseline”. Furthermore, there is little accuracy between data on the suction surface from 25% to 50% of chord. The experimental data shows a sinusoidal pattern, but the CFD shows a flat pattern. However, it should be noted that, according to Schreiber [10], this discrepancy was caused by some disturbances emanating from the blade leading edge sidewall corner region, where the detached bow shock interacts



**Fig. 4 Experimental shock wave pattern for “baseline” cascade at near design condition,  $M_1=1.45$ ,  $P_{s2}/P_{s1}=2.21$ ,  $AVDR=1.01$ ; obtained from Schreiber [22]**



(a)



(b)

**Fig. 5 Simulated Schlieren pictures for “baseline” cascade at near design condition,  $M_1=1.457$ ; (a) Overall, (b) Detail of LE part**



with the incoming sidewall boundary layer. These disturbances are weak three-dimensional compression and expansion waves and fade away towards the blade mid-span height. However, a minor influence on the blade suction surface flow remains. This may be the cause of the quantitative discrepancy between EXP and CFD in this region.

Figure 7 shows wake traverse data, corresponding to the total pressure loss coefficient: (Fig. 7-(a)) and the exit flow angle (Fig. 7-(b)). Again the experimental data of both loss and flow angle have been taken from Küsters and Schreiber [11]. The pitch-wise position of the numerical data of loss and flow angle has been adjusted to have the peak loss at the pitch-wise direction of  $y/s = 0.0$  where the experimental data has the peak value. Regarding the total pressure loss distribution, there is a good qualitative agreement between EXP and CFD where a second peak loss observed in EXP is predicted as a “bulge” pattern in CFD. The reason for the second peak loss will be discussed in the Section “Optimized Airfoil and Flow Mechanism”.

There is a considerable difference between EXP and CFD for the viscous loss region around  $-0.1 < y/s < +0.1$  originating from the airfoil boundary layers, as well as for the shock losses outside of the wake around  $+0.1 < y/s < +0.3$  (see Fig. 7-(a)). One reason could be the difference between the AVDR values in EXP (1.06) and CFD (1.00). According to Schreiber [22], increasing stream tube contraction (higher AVDR) causes a slight upstream shifting of the passage shock waves, when the back pressure is forced to be constant. Thereby, the shock strength decreases resulting in a considerable relaxation of the strong interaction process. There is also a quantitative discrepancy between EXP and CFD for the exit flow angle distribution (see Fig. 7-(b)). The CFD shows about one degree of under-turning compared to the EXP. The reason is probably the difference of the AVDR values.

As a brief summary, the CFD simulations used in this research predict the complex flow phenomena observed in the experimental results qualitatively well, although some quantitative discrepancies remain.

### Optimized Airfoil and Flow Mechanism

The airfoil geometry resulting from the optimization method ES is shown together with the “baseline” profile in Fig. 8. The left side in Fig. 8 shows the overall geometries for the “baseline” (black) and the “optimized” (red) blade. On the right hand side close-ups of the LE regions of the two airfoils are shown. The optimized airfoil is thicker around the rear portion compared to the “baseline” cascade and the LE profile is very unique. The thickness distributions of the two airfoils are compared in Fig. 9. The position of maximum thickness for the “optimized” cascade is significantly shifted toward downstream ( $x/c \approx 0.31 \rightarrow 0.37$ ; i.e., from about 60% to about 70% of fraction of chord length). The maximum thickness is larger for

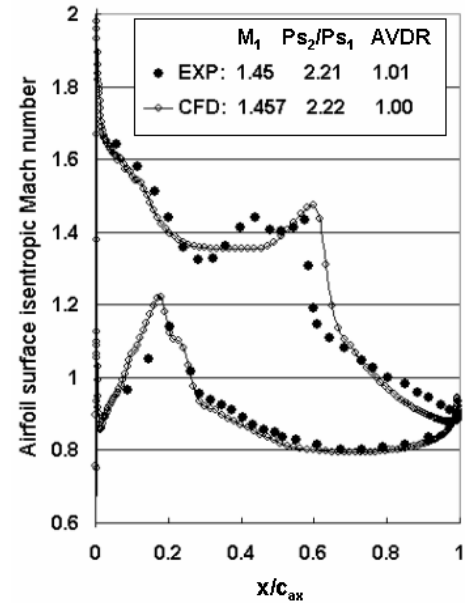


Fig. 6 Comparison of “measured” and “calculated” isentropic airfoil surface Mach number distribution for “baseline” cascade; EXP is obtained from Schreiber [22]

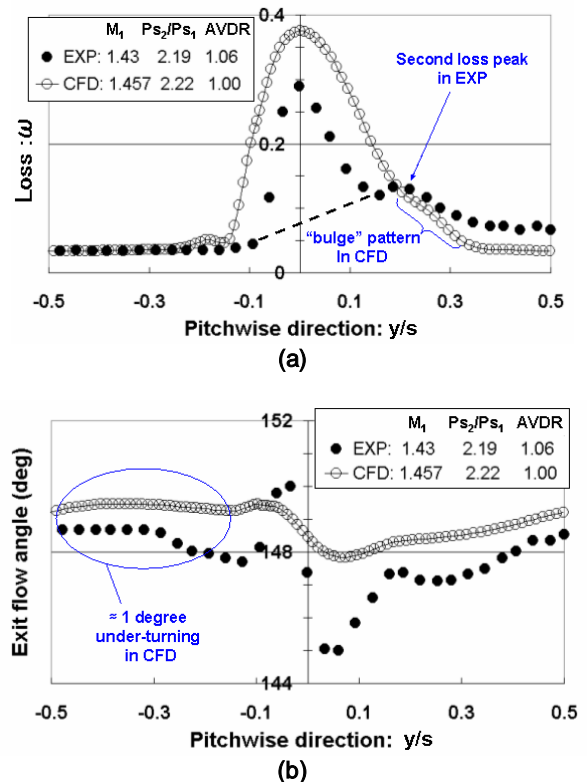


Fig. 7 Pitch-wise distribution at 28% axial chord behind TE for “baseline” cascade; (a) Total pressure loss coefficient, (b) Exit flow angle; EXP is obtained from Küsters and Schreiber [11]



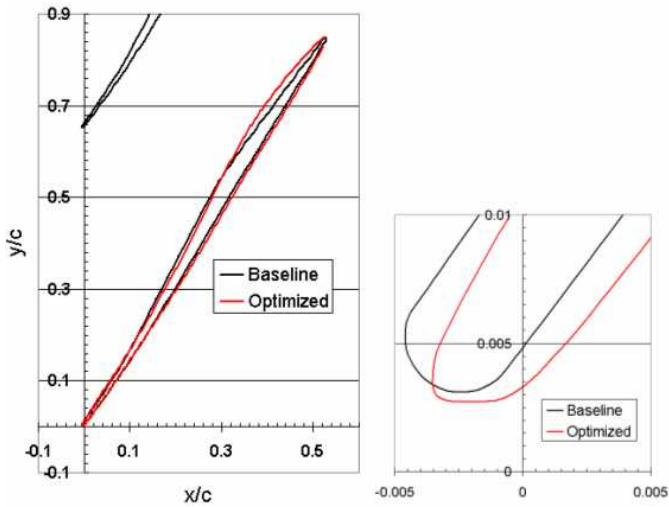


Fig. 8 Comparison of airfoil geometries for “baseline” and “optimized”; overall view (left), details of LE (right)

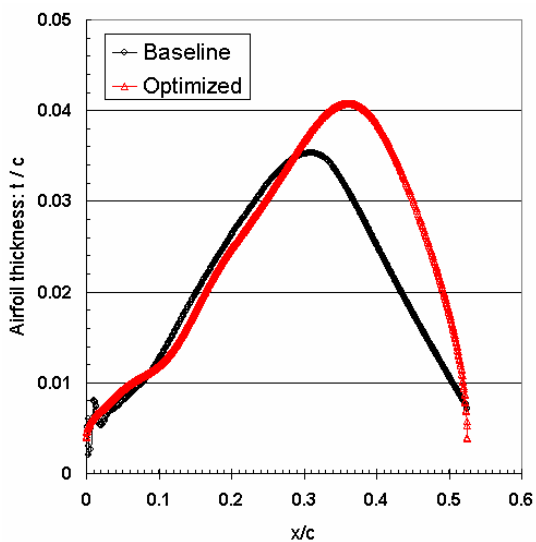


Fig. 9 Comparison of airfoil thickness distribution for “baseline” and “optimized” cascades

the “optimized” blade:  $t/c \approx 0.035$  (baseline)  $\rightarrow 0.041$  (optimized). The comparison of the computed parameters for the “baseline” and the “optimized” cascades is shown in Table 2 (see “CFD”). The inlet Mach number for the optimized cascade is slightly increased and the incidence angle is significantly decreased about 1 degree compared to the “baseline” cascade. The optimized blade has a higher static pressure ratio and a lower loss.

The simulated Schlieren picture for the “optimized” cascade is presented in Fig. 10. There are some interesting differences to the “baseline” cascade (see also Fig. 5). Firstly, the expansion wave region around the LE in the “optimized”

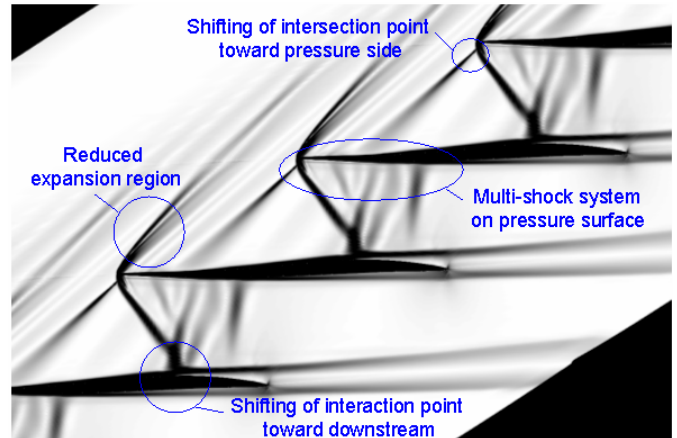


Fig. 10 Simulated Schlieren picture for “Optimized” cascade at near design condition;  $M_1=1.508$ ,  $P_{s2}/P_{s1}=2.32$

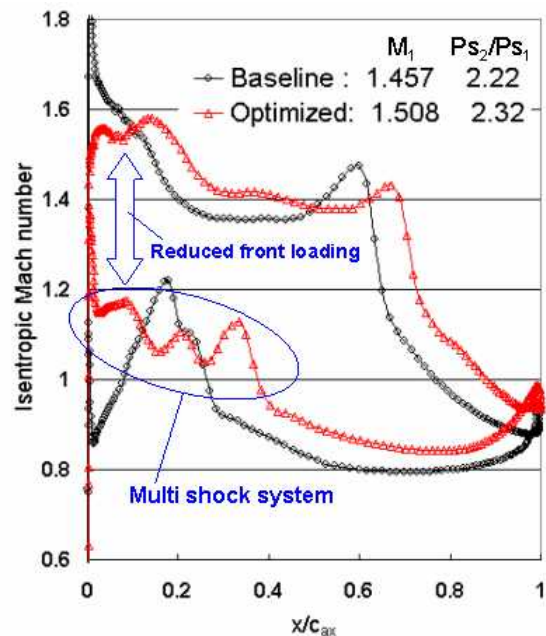


Fig. 11 Airfoil surface isentropic Mach number distribution for “baseline” and “optimized” cascades

cascade is significantly reduced. Secondly, the intersection of the pre-compression shock with the bow shock observed around the suction-side LE in the “baseline” cascade is shifted toward the pressure-side. As a result, the pre-compression shock hits the first passage shock. Thirdly, there seems to be a multi-shock system around the front portion on the pressure-side, and finally the shock/boundary layer interaction point is slightly shifted downstream.

The airfoil surface isentropic Mach number distribution for the “optimized” cascade is shown together with the “baseline” cascade profile in Fig. 11. There are two interesting observations. The first is the loading level around LE portion

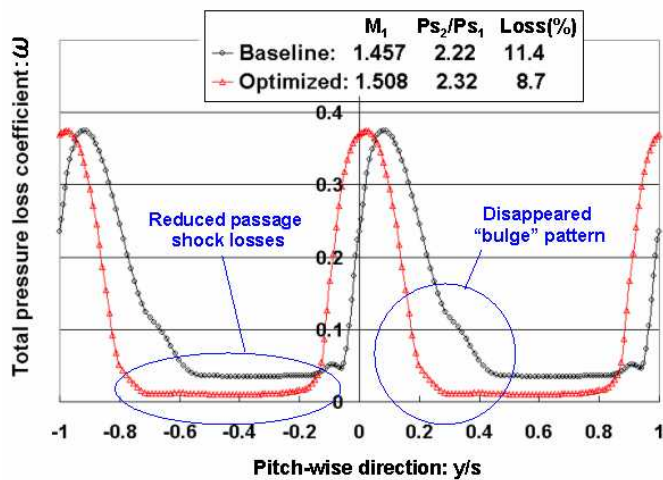


Fig. 12 Comparison of pitch-wise loss distribution for “baseline” and “optimized” cascades

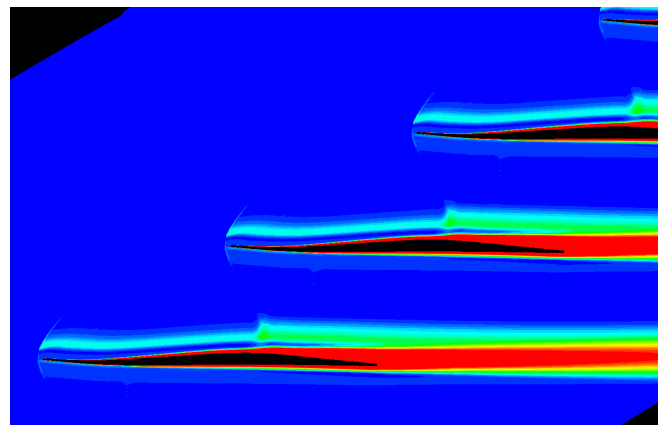
( $0 < x/c_{ax} < 0.1$ ) for the “optimized” cascade. Compared to the “baseline” this value is dramatically reduced. This reduction may be preferable for surge margin, because Wadia and Law [23] reported in their three-dimensional calculation that the leading edge loading at the rotor tip section was increased at near stall.

The second interesting observation is a velocity zigzag pattern around the front portion on the pressure surface ( $0 < x/c_{ax} < 0.4$ ). As already shown in the simulated Schlieren picture (see Fig. 10) there are some weak shocks, i.e., a multi-shock system, instead of the second passage shock observed in the “baseline” cascade. The multi-shock system seems to result in a smooth deceleration with lower shock losses compared to the “baseline” cascade. Therefore, the multi-shock system is useful to avoid a strong passage shock called the second passage shock and as such it may be a good design concept.

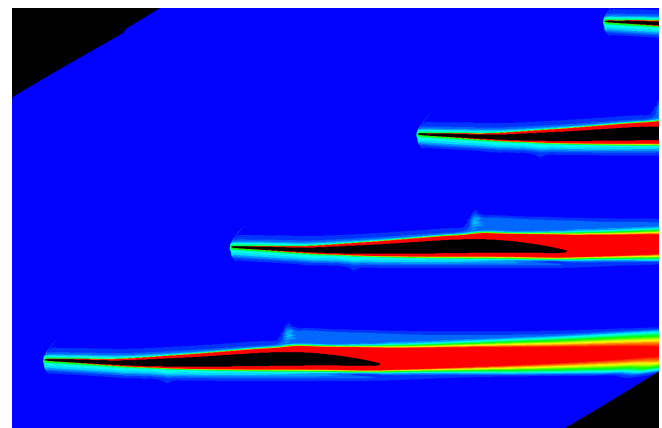
The chord-wise location of the first passage shock is slightly shifted toward downstream (from 60% to 67% of axial chord) and the peak Mach number is significantly reduced from 1.48 to 1.43 resulting in a weaker shock.

Figure 12 shows a comparison of pitch-wise total pressure loss coefficients for both “baseline” and “optimized” cascades. In the case of the “baseline” cascade, we observe the “bulge” pattern, corresponding to the second peak loss in EXP on the suction-side, as already described in the previous section. In the case of the “optimized” cascade, there is no “bulge” pattern and the total pressure loss coefficient in the free wake is significantly reduced (from 3.4% to 1.0%).

The “bulge” pattern was also reported by Kunz and Lakshminarayana [24] and by Küsters and Schreiber [11] in their Navier-Stokes computations. Kunz and Lakshminarayana [24] suggested that the second peak loss (“bulge” pattern in CFD) can be attributed to the lambda shock system generated by the first passage shock/boundary layer interaction. At the same time, Küsters and Schreiber [11] reported using total



(a)



(b)

Fig. 13 Entropy contours for “baseline” and “optimized” cascades; (a) baseline, (b) optimized

pressure contour data that the second peak loss also originates far upstream near the leading edge, where the oblique pre-compression shock intersects the detached bow shock.

In order to identify the cause of the “bulge” pattern (the second peak loss in EXP), the entropy pattern has been investigated. Figure 13 shows the entropy contours for both cascades. There is no large difference in the first passage shock/boundary layer interaction (red color), which was to be expected from the airfoil isentropic Mach number distribution (see Fig. 11). However, there is a large difference in the second peak loss between the two cascades.

In the case of the “baseline” cascade, the second peak loss observed in EXP has the origin at the intersection point (right blue), where the pre-compression shock impinges on the bow shock. The “right-blue” entropy line along the suction surface away from the surface impinges on the first passage shock and then it spreads out due to the normal part of the lambda shock above the shock induced separation (green). These results support Küsters and Schreiber’s [11] observation.

In the case of the “optimized” cascade, there is no high entropy region on the suction surface corresponding to the second peak loss due to the shifting of the intersection from the suction side to the pressure side, as already shown in the simulated Schlieren picture (see Fig. 10). This is the reason why the second peak loss was observed in the “baseline” experiment. The influence of the pressure-side intersection point for the “optimized” cascade, generated by the pre-compression shock and the first passage shock, is observed along the pressure surface (right-blue). However, the influence on the total pressure losses is very small (see Fig. 12). The reason for this seems to be the existence of a multi-shock system having a relatively weak shock strength.

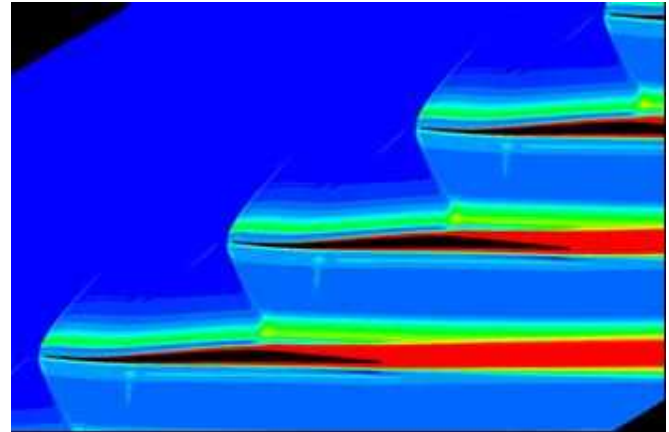
Figure 14 (a) and (b) show the total pressure loss contours for the “baseline” and “optimized” cascades, respectively. In the case of the “baseline” cascade there is a high loss region just downstream of the first passage shock, while there is no high loss region for the “optimized” cascade. This is the reason why a large reduction of the loss in the free wake was observed for the “optimized” cascade (see Fig. 12).

Although confirmation by experiments of the presented optimization results for the supersonic cascade is needed for final verification, we are confident that - at least qualitatively - the results will carry over to the experiment. This confidence is rooted in the successful comparison of the used flow solver HSTAR with experimental data, which we discussed in the paper.

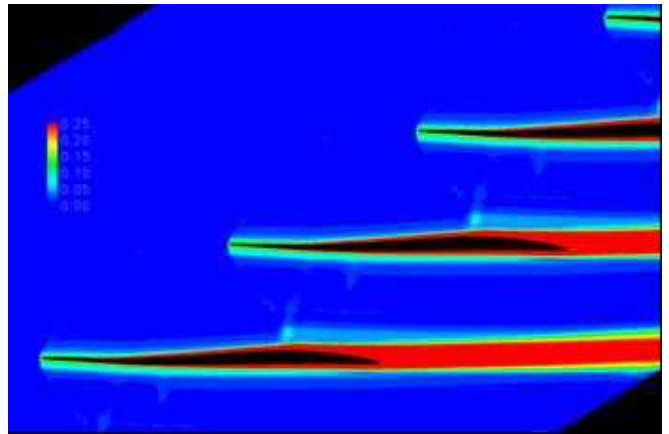
## CONCLUSIONS

In this study, a numerical shape optimization method based on evolutionary algorithms coupled with a verified CFD solver have been applied to the minimization of the shock of a 2-D supersonic inlet Mach number compressor cascade, using the DLR-PAV-1.5 supersonic compressor cascade designed by a pre-compression blading concept as a baseline. The target has been to investigate the supersonic flow field with accompanying shock waves and to possibly identify new design concepts. The following conclusions can be drawn:

- The optimized airfoil has a unique leading edge geometry and the location of the point of maximum thickness is shifted toward downstream from about 60% to 70% of fraction of chord length having a thicker distribution around the rear portion compared to the DLR-PAV-1.5 “baseline” cascade.
- The “optimized” cascade shows superior performance with about 24% reduction of the total pressure loss coefficient compared to DLR-PAV-1.5.
- The loss improvement observed in the “optimized” cascade is mainly due to a weaker first passage shock loss and the absence of a second peak loss which is only visible in the DLR supersonic cascade testing (“bulge” pattern in CFD).



(a)



(b)

**Fig. 14 Total pressure loss contours for “baseline” and “optimized” cascades; (a) baseline, (b) optimized**

- The reason for the absence of the second peak loss lies in the shifting of an intersection point of a pre-compression shock with a bow shock from the suction-side to the pressure-side.
- In the “optimized” cascade there is no high entropy region along the pressure surface, although the intersection point of the pre-compression shock with the first passage shock was shifted to the pressure-side. The reason seems to be a multi-shock system instead of the strong second passage shock observed in the baseline.

## OUTLOOK

In this optimization, there is still room for improvement to reduce the total pressure loss even further. Because the zigzag pattern of the Mach number observed on the frontal pressure surface, especially the “increase” pattern is not preferable. Also, there is still a strong shock/boundary layer interaction in the first passage shock. We will concentrate on these two points next.

## ACKNOWLEDGMENTS

The authors would like to thank Heinz-Adolf Schreiber from the DLR for his helpful comments during the study and the preparation of the manuscript and for providing the detailed blade geometry of DRL-PAV-1.5.

## REFERENCES

- [1] Mohammed, K.P. and Raj, D., 1977, "Investigation on Axial Flow Fan Impellers with Forward Swept Blades", ASME paper No. 77-FE-1.
- [2] Wadia, A.R., Szucs, P.N. and Crall, D.W., 1997, "Inner Workings of Aerodynamic Sweep", ASME Paper 97-GT-401, see also ASME Journal of Turbomachinery, 120, pp. 671-682.
- [3] Denton, J.D. and Xu, L., 2002, "The Effects of Lean and Sweep on Transonic Fan Performance", ASME Paper GT2002-30327.
- [4] Beyer, H.-G. and Schwefel, H.-P., 2002, "Evolution strategies - A comprehensive introduction. Natural Computing, Vol. 1, No. 1, pp. 3-52.
- [5] Sonoda, T., Yamaguti, Y., Arima, T., Olhofer, M., Sendhoff, B., Schreiber, H. A., 2004, "Advanced High Turning Compressor Airfoils for Low Reynolds Number Condition, Part 1: Design and Optimization", ASME Journal of Turbomachinery, Vol. 126, No. 3, pp. 350-359.
- [6] Sonoda, T. and Schreiber, H.A., 2007, "Aerodynamic Characteristics of Supercritical Outlet Guide Vanes at Low Reynolds Number Conditions", ASME Journal of Turbomachinery, Vol. 129, pp. 694-704.
- [7] Sonoda, T., Arima, T., Olhofer, M., Sendhoff, B., Kost, F., and Giess, P.-A., 2006, "A Study of Advanced High-Loaded Transonic Turbine Airfoils", ASME Journal of Turbomachinery, Vol. 128, No. 4, pp. 650-657.
- [8] Morris, A.L., Halle, J.E., and Kennedy, E., 1972, "High-Loading, 1800 ft/sec Tip Speed Transonic Compressor Fan Stage, 1. Aerodynamic and Mechanical Design", NASA CR-120907, PWA-4534.
- [9] Schreiber, H.A., 1987, "Experimental Investigations on Shock Losses of Transonic and Supersonic Compressor Cascades", AGRAD CP-401, Paper 11.
- [10] Schreiber, H.A., Starken, H., 1992, "An Investigation of a Strong Shock-Wave Turbulent Boundary Layer Interaction in a Supersonic Compressor Cascade," ASME Journal of Turbomachinery, Vol. 114, pp. 494-503.
- [11] Küsters, B. and Schreiber, H.A., 1998, "Compressor Cascade Flow with Strong Shock-Wave/Boundary-Layer Interaction", AIAA Journal, Vol. 36, No. 11, pp. 2072-2078.
- [12] Hansen, N. and Ostermeier, A., 2001, "Completely Derandomized Self-Adaptation in Evolution Strategies". Evolutionary Computation, Vol 9, No. 2, pp. 159-195.
- [13] Jastrebski, G.A. and Arnold, D.V., 2006, "Improving Evolution Strategies through Active Covariance Matrix Adaptation", IEEE Congress on Evolutionary Computation, pp. 2814 – 2821.
- [14] Hasenjäger, M., Sendhoff, B., Sonoda, T. and Arima, T., 2005, "Three dimensional evolutionary aerodynamic design optimization with CMA-ES", Proceedings of the Conference on Genetic and Evolutionary Computation, pp. 2173-2180.
- [15] Hüsken, M., Jin, Y. and Sendhoff, B., 2005, "Structure Optimization of Neural Networks for Evolutionary Design Optimization", Soft Computing Journal, Vol. 9, No. 1, pp. 21-28.
- [16] Jin, Y., Olhofer, M. and Sendhoff, B., 2002, "A framework for evolutionary optimization with approximate fitness functions", IEEE Transactions on Evolutionary Computation Vol. 6, No. 5, pp. 481-494.
- [17] Pierret, S. and van den Braembussche, R.A., 1999, "Blade Design Using a Navier–Stokes Solver and Artificial Neural Network", Journal of Turbomachinery, Vol. 121, No. 2, pp. 326-332.
- [18] Beyer, H.-G. and Sendhoff, B., 2007, "Robust optimization - A comprehensive survey", Computer Methods in Applied Mechanics and Engineering, Vol. 196, No. 33-34, pp. 3190-3218.
- [19] Beyer, H.-G. and Sendhoff, B., 2006, "Functions with Noise-Induced Multi-Modality: A Test for Evolutionary Robust Optimization - Properties and Performance Analysis", IEEE Transactions on Evolutionary Computation, Vol 10, No. 5, pp. 507-526.
- [20] Arima, T., Sonoda, T., Shiratori, M., Tamura, A., Kikuchi, K., 1999, "A Numerical Investigation of Transonic Axial Compressor Rotor Flow Using a Low Reynolds number k- $\epsilon$  Turbulence Model", ASME Journal of Turbomachinery, Vol. 121, No.1, pp. 44-58.
- [21] Chien, J.Y., 1982, "Prediction of Channel and Boundary Layers With a Low-Reynolds-Number Two Equation Model of Turbulence", AIAA Journal, Vol. 20, pp.33-38.
- [22] Schreiber, H.A., 1995, "Shock-Wave Turbulent Boundary Layer Interaction in a Highly Loaded Transonic Fan Blade Cascade", AGARD CP-571, Paper No. 17.
- [23] Wadia, A.R. and Law, C.H., 1993, "Low Aspect Ratio Transonic Rotors: Part 2-Influence of Location of Maximum Thickness on Transonic Compressor Performance", ASME Journal of Turbomachinery, Vol. 115, pp. 226-239.
- [24] Kunz, R.F. and Lakshminarayana, B., 1992, "Explicit Navier-Stokes Computation of Cascade Flows Using the k- $\epsilon$  Turbulence Model", AIAA Journal, Vol. 30, No. 1, pp. 13-22.